UKAEA-CCFE-PR(22)42

Lei Tang, Fuqing Jian, Yiqiang Wang, Saurabh Kabra, Biao Cai

Mechanical performance and deformation mechanisms at cryogenic temperatures of 316L stainless steel processed by laser powder bed fusion: in situ neutron diffraction

Enquiries about copyright and reproduction should in the first instance be addressed to the UKAEA Publications Officer, Culham Science Centre, Building K1/0/83 Abingdon, Oxfordshire, OX14 3DB, UK. The United Kingdom Atomic Energy Authority is the copyright holder.

The contents of this document and all other UKAEA Preprints, Reports and Conference Papers are available to view online free at scientific-publications.ukaea.uk/

Mechanical performance and deformation mechanisms at cryogenic temperatures of 316L stainless steel processed by laser powder bed fusion: in situ neutron diffraction

Lei Tang, Fuqing Jian, Yiqiang Wang, Saurabh Kabra, Biao Cai

This is a preprint of a paper submitted for publication in
Scripta materialia

Mechanical performance and deformation mechanisms at cryogenic temperatures of 316L stainless steel processed by laser powder bed fusion: *in situ* neutron diffraction

Lei Tang[a], Oxana V. Magdysyuk[b], Fuqing Jiang[c], Yiqiang Wang[d], Alexander Evans[e], Saurabh Kabra[f], Biao Cai[a*]

[a] School of Metallurgy and Materials, University of Birmingham, B15 2TT, United Kingdom
[b] Diamond Light Source Ltd, Harwell Science and Innovation Campus, Didcot, United Kingdom
[c] Institute of Metal Research, Chinese Academy of Sciences, Shenyang 110016, China
[d] United Kingdom Atomic Energy Authority, Culham Science Centre, Abingdon OX14 3DB, United Kingdom
[e] Division 8.5 Micro Non-Destructive Testing, Bundesanstalt für Materialforschung und –prüfung (BAM), Unter den Eichen 87, 12205 Berlin, Germany
[f] ISIS Facility, Rutherford Appleton Laboratory, Didcot OX11 0QX, United Kingdom
* Corresponding author
E-mail address: b.cai@bham.ac.uk

Abstract

Manufacturing austenite stainless steels (ASSs) using additive manufacturing is of great interest for cryogenic applications. Here, the mechanical and microstructural responses of a 316L ASS built by laser powder-bed-fusion were revealed by performing *in situ* neutron diffraction tensile tests at the low-temperature range (from 373 to 10 K). The stacking fault energy almost linearly decreased from 29.2±3.1 mJm^{-2} at 373 K to 7.5±1.7 mJm^{-2} at 10 K, with a slope of 0.06 $mJm^{-2}\cdot K^{-1}$, leading to the transition of the dominant deformation mechanism from strain-induced twinning to martensite formation. As a result, excellent combinations of strength and ductility were achieved at the low-temperature range.

Keywords

Additive manufacturing; cryogenic deformation; neutron diffraction; austenitic stainless steel

With valuable combinations of excellent corrosion/oxidation resistance and strength-ductility balance, austenitic stainless steels (ASSs) serve as workhorse materials in various cryogenic applications such as liquified gas storage/transportation, superconductivity realization, rocket propellant tanks and nuclear fusion devices [1,2]. Recently, ASSs have been gaining enormous research interests as a desirable material for additive manufacturing (AM), which fabricates 3-dimensional components layer-by-layer thus enabling significant weight reduction and complex geometrical design [3,4]. ASSs fabricated by laser powder-bed-fusion (L-PBF), yields superior mechanical performance [5,6] originated from a variety of concurrent strengthening effects including dislocation slips, twinning, and strain-induced martensite transformation (SIMT), where the parent face-centered cubic (FCC) matrix (γ-austenite) can undergo an athermal transition into martensite with hexagonal close-packed (ε) or body centered-tetragonal (α′) structures. These strengthening mechanisms are strongly dependent on the stacking fault energy (SFE), which is an inherent parameter measuring the energy barrier of dissociating perfect dislocations and can be influenced by chemical composition, strain rate, and temperature [7–9]. The decreasing of SFE can shift the dominant deformation mechanisms from dislocation motion (SFE > 45 mJm^{-2}) to twinning (45 mJm^{-2} > SFE > 18 mJm^{-2}) and to SIMT (SFE < 18 mJm^{-2}) [9–11].

The relationship among SFE, temperature, and the deformation mechanisms in the ASSs fabricated by AM, however, was still under debate. Pham et al. [12] reported the reduced SFE of a 316L ASS after L-PBF compared to conventional 316L ASS, which is attributed to the diffusion of N atoms to the faulted structures. Contrarily, Karthik [2] reported the increased SFE after L-PBF due to the cellular dislocation structures. A similar phenomenon was also reported in another L-PBF-built 316L ASS during cryogenic deformation [6], where SIMT was significantly postponed compared with the annealed counterparts. In addition, most of the previous investigations focused on the high or room-temperature performance of the AM-fabricated ASSs, while the SFE-related mechanical responses and strengthening effects at ultralow temperatures, have rarely been investigated, which severely limited the application of L-PBF build ASSs for cryogenic environments.

Herein, *in situ* neutron diffraction and tensile tests were performed on an L-PBF-built 316L ASS at the low-temperature range (from 373 to 10 K), providing a better understanding of the relationship among SFE, temperature, and deformation mechanisms of AM-built ASSs and thus paving a way to develop ASSs fabricated by L-PBF with superior cryogenic mechanical properties.

Near spherical-shaped 316L powder with a diameter of 32±5 μm was prepared by gas atomization. Specimens with a size of $100 \times 40 \times 40$ mm^3 were manufactured in an L-PBF machine (FS271M, Farsoon, China) under the protection of nitrogen atmosphere and then annealed at 400 ℃ for 3 h, followed by air cooling. The printing parameters are listed in Table. 1. The laser beam was rotated 67° after printing each layer. Dog-bone tensile samples (with gauge volume of Φ 8 × 32 mm^3) were then machined along the building direction and used for the *in situ* tensile testing. The tensile tests (with a strain rate of 9×10^{-4} S^{-1}) were performed using an Instron stress rig with a high-vacuum (< 10^{-5} Pa) chamber. The stress rig was mounted horizontally and 45° to the incident beam. Two detectors were mounted perpendicular to the incident beam and can collect the diffraction patterns from the tensile and transverse directions. Diffraction patterns were collected for 15 mins intervals between loading steps, iterating until sample fracture. The details of *in situ* neutron diffraction tensile testing and related data interpretation, such as the calculation of lattice strain, dislocation density, stacking fault probability (SFP), and SFE can be found at Refs. [7,8,13,14]. The neutron diffraction data were analyzed by Rietveld refinement [15,16] using the TOPAS program [17], which allows to refine the weight fraction and the preferred orientation of each phase by applying the same functions that are widely used for analysis of X-ray diffraction data. The lattice strain for ε-martensite was not refined to avoid data overfitting due to much broader peaks of this phase in comparison with other two phases. The lattice strain for α′-martensite was refined only for a few data sets for which the amount of α′-martensite was considerable. The comparison between the measured two diffraction patterns collected during deforming at 10 K and the corresponding Rietveld refinement results was shown in Fig. S1 of the Supplementary

Materials. The electron back scatter diffraction (EBSD) was performed at the plane perpendicular to the building direction on a scanning electron microscope (SEM, Tescan Mira-3) with an accelerating voltage of 15 kV. The thin foils for transmission electron microscope (TEM) characterization were mechanically polished to ~80 μm and then subjected to twin-jet electropolishing using a constant current of 150 mA in a solution of 5% perchloric acid and 95% methanol cooled to -30 °C. The TEM observation was performed on a Tecnai G^2 F30 TEM operated at 300 kV.

Table. 1 Parameters used in building 316L ASS with L-PBF

Scanning speed [mm·s^{-1}]	Laser beam spot size [μm]	Laser power [W]	Layer thickness [μm]	Hatching space [μm]
1000	80	225	30	90

In Fig. 1 the heterogeneous distribution of grain shape/size and orientation gradient of the as-built 316L ASS were revealed with EBSD and bright-field TEM image. The inverse pole figure (IPF) shows multiple ripple patterns consisting of large elliptic grains and slim grains distributing along the melt pool boundaries (Fig. 1a). The average grain size (d) of 19.5 μm was determined with the intercept length method. Unconventional orientation gradient across grains was observed and shown as a high-resolution kernel average misorientation map in Fig. 1b. The local misorientation within the large grain interior was in the range of 0.5°-1.5°, while the high local misorientation (> 2°) was preferably located in slim grains or around (sub)grain boundaries. The misorientation distribution was compared with random misorientation [18] in Fig. 1c, showing a very high fraction of low angle grain boundaries (LAGBs, $2° < \theta < 10°$, 67.7% of the total grain boundaries). The bright-filed TEM image in Fig. 1d reveals the densely arrayed dislocation cells (~200 nm in width and ~500 nm in length) within the grain interior, which can be the origin of the high fraction of LAGBs and high level of local misorientation. A high density of dislocations trapping within/along the fine dislocation cells are visible and induced dislocation entanglements (Fig. 1d).

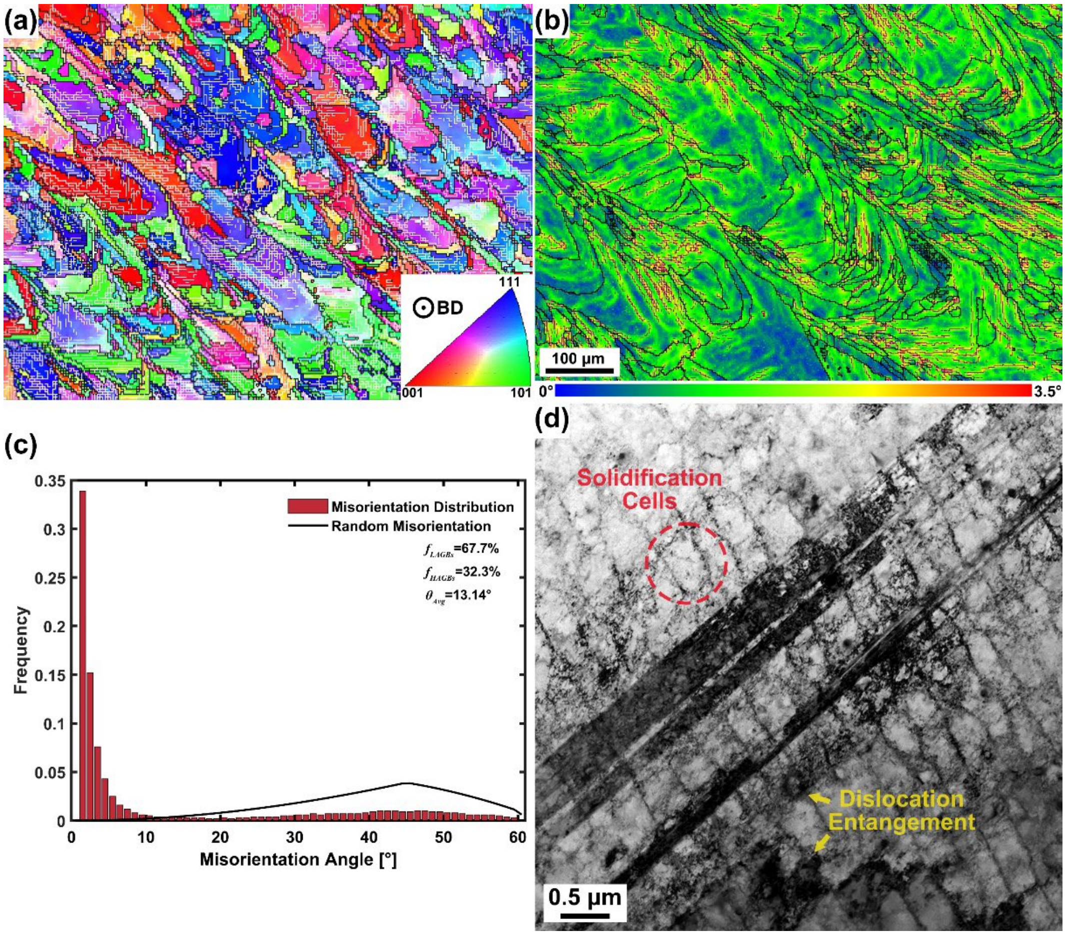
(a)
BD
111
001
101
(b)
100 μm
0°
3.5°
(c)
Misorientation Distribution
Random Misorientation
f_{LAGBs}=67.7%
f_{HAGBs}=32.3%
θ_{Avg}=13.14°
Frequency
0
0.05
0.1
0.15
0.2
0.25
0.3
0.35
0
10
20
30
40
50
60
Misorientation Angle [°]
(d)
Solidification Cells
Dislocation Entangement
0.5 μm

Fig. 1 Initial microstructure of the as-built 316L ASS revealed by EBSD and TEM characterization: (a) inverse pole figure (IPF) map took at the plane perpendicular to the building direction, low angle grain boundaries (LAGBs, 2° < θ < 10°) and high angle grain boundaries (HAGBs, θ > 10°) were shown with white and black lines, respectively; (b) high-resolution kernel average misorientation map showing orientation gradient, (c) Misorientation distribution of the sample compared with theoretical random misorientation from Ref. [15], and (d) typical bright-field TEM image. BD denotes the building direction.

The temperature-dependent mechanical performance of the steel was presented in Fig. 2. Fig. 2a shows the representative true stress-strain curves, which shows typical parabolic patterns when the temperature is higher than 173 K and progressively evolves to sigmoidal/S-shaped type as temperature decreased to the ultra-low temperature range (< 173 K). With the decrease of temperature, the yield strength (YS) of the steel increased almost linearly from 562 MPa at 373 K, reaching its peak of 935 MPa at 10 K. The ultimate tensile strength (UTS) was also enhanced significantly from 627 MPa at 373 K to 1364 MPa at 10 K. The elongation was 55% at 373 K and maintained at a high level of ~35% at cryogenic temperatures. The strain hardening rate (SHR, $d\sigma/d\varepsilon$) (Fig. 2c) can be roughly divided into three stages. At Stage I, SHR exhibited a steep decrease to a very low level (< 2 GPa) due to the elastic-plastic transition [19]. Afterwards, the SHR curves increased to a peak value at Stage II, indicating new sources contributing to strain hardening, followed by continuous decreasing until fracture (Stage III). The transition points from Stage I to Stage II were also marked with dash lines. The strain hardening effects mainly occurred at

Stage II and can be significantly enhanced by decreasing the temperature. The peak value of SHR at Stage II was only 0.98 GPa at the strain of 0.17 at 373 K and boosted to 6.25 GPa at 0.29 strain level at 10 K.

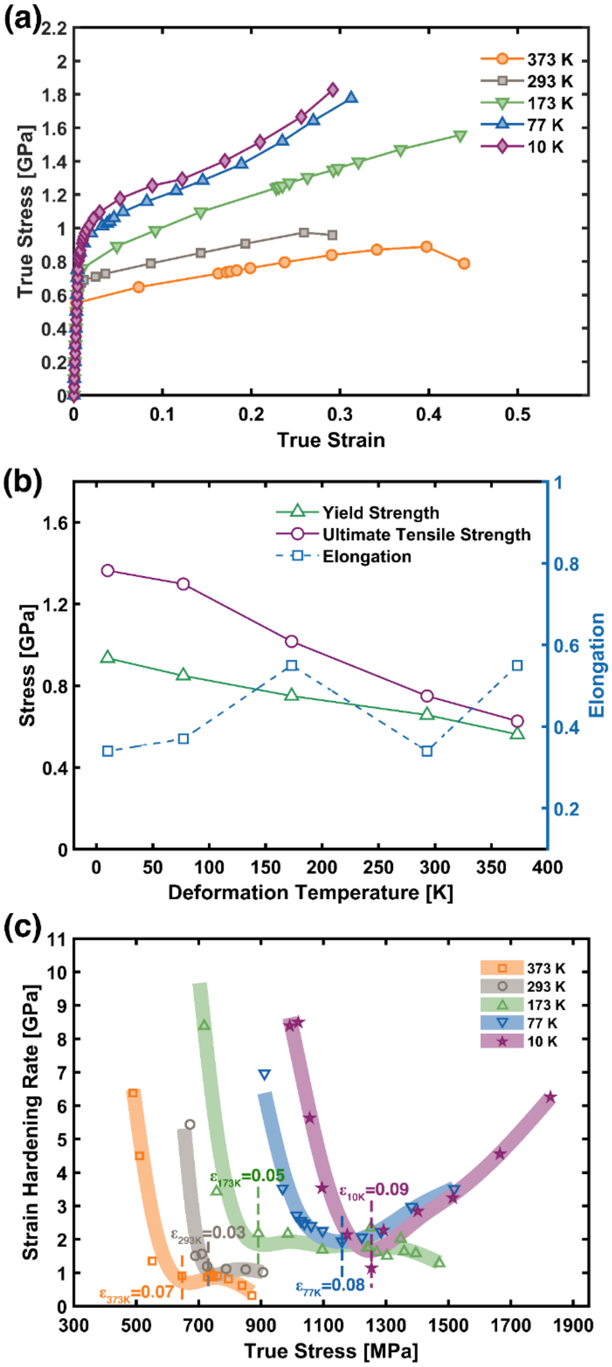

Fig. 2 Mechanical performance of the 316L ASS at the low temperature range: (a) true stress-strain curves, (b) evolution of mechanical properties with respect to deformation temperature, and (c) strain hardening rate (SHR) plotted with true stress. The SHR transition points from Stage I to Stage II (ε_{373K}, ε_{293K}, ε_{173K}, ε_{77K}, and $\varepsilon_{10\,K}$) were marked with dashed lines.

The diffraction spectra collected from tensile direction during deformation at different temperatures were plotted as a function of true stress in Fig. 3. The as-built steel exhibited an FCC structure with decreasing lattice parameters (a_0, Table S1 of the Supplementary Materials) during the temperature decreasing stage. SIMT only occurred when deforming at 173 K or lower (Fig. 3c-f), as three new diffraction peaks emerged and grew with strain, which can be identified as α′-(110), α′-(211), and ε-(10$\bar{1}$1). The diffraction patterns at 10 K were magnified in Fig. 3f, showing the intensity of the α′-(111) increased progressively with straining while the peak intensity of γ-(111) and γ-(200), decreased contrarily.

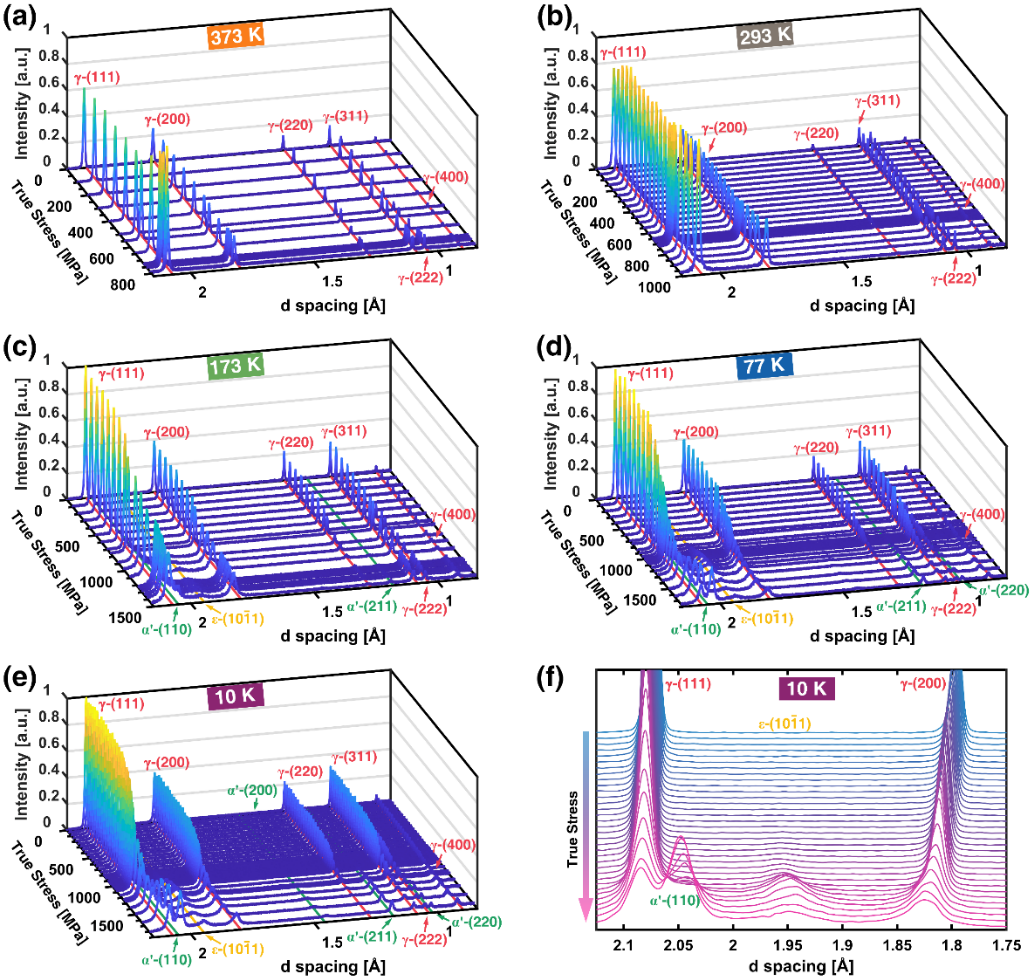

Fig. 3 The *in situ* neutron diffraction patterns (loading direction) collected during deforming at different temperatures: (a) 373 K, (b) 293 K, (c) 173 K, (d) 77 K, (e) 10 K, and (f) 10 K, with higher magnification.

Lattice strain evolution at tensile and transverse directions during deformation at different temperatures was shown in Fig. 4a-d. The lattice strain evolution at 77 and 10 K was plotted only at the low strains. This is because the overlap of diffraction peaks of γ and α′ phases can cause high ambiguity in determining lattice strain using the peak position. During the elastic stage, the varied stiffness of the reflection indicated the load redistribution among grains. The {200} grain family shows the lowest diffraction elastic moduli (softest) and the highest lattice strain (Fig. 4a-d). Before the macroscopic yielding, the non-linear relationship was also observed due to the stress transferred from some stiff grains (e.g., 220) to soft grain families (e.g., 200) [20]. After macroscopic yielding, the evolution of lattice strain is highly anisotropic, indicating the redistribution of the stress or the reorientation of crystals.

The lattice strain evolution at tensile and transverse directions were applied to determine the macroscopic and *hkl*-specific elastic moduli (See details at Ref. [7] and results in Table S1 of the Supplementary Materials). The *hkl*-specific elastic moduli were then applied to determine the single-crystal elastic constants (C_{11}, C_{12}, and C_{44}) with the Kroner model [21] and details can be found at Refs. [21–23]. C_{11}, C_{12}, and C_{44} values are consistent with literature data of 316L stainless steel [24]. They increase gradually as the temperature decreases.

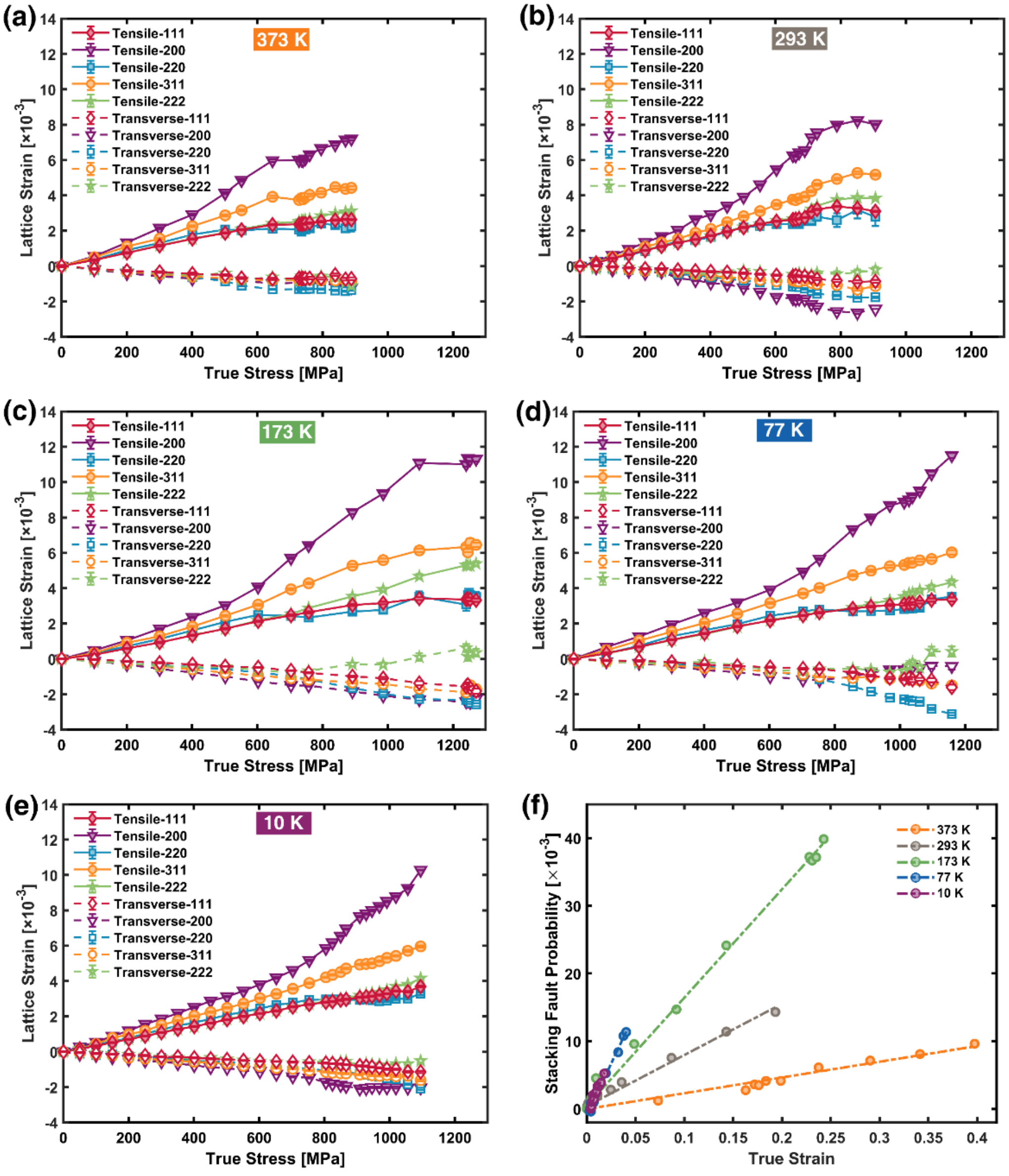

Fig. 4 The evolution of (a-e) lattice strain of crystallographic planes {111}, {200}, {220}, {311}, and {222} at the tensile and transverse direction and (f) stacking fault probability evolution during deforming at 373, 293, 173, 77, and 10 K.

The SFP, which indicates the amount of SFs, can be determined by the separation distance of lattice strain of two consecutive grain planes (See details in Refs. [7,13]). Considering the low intensity of the (200) and (400) peak in the present study (Fig. 3), we chose the lattice strain of (111) and (222) grain planes to determine the SFP. The SFP evolution at different temperatures were plotted in Fig. 4f. SFP showed a nearly linear increase with true strain, whereas the slope of the fitted line ($\partial SFP/\partial \varepsilon$) depicts the speed of SFs formation. At 373 K SFs gathered with a very slow pace with $\partial SFP/\partial \varepsilon$ of 23.2×10^{-3}, which boosted to 360.1×10^{-3} at 10 K. The SFE was then calculated according to Refs. [7,13,25]. The evolution of SFE with true strain at 293 K was shown in Fig. S2 of the Supplementary Materials. The SFE started from a very high value of ~110 mJm^{-2} and continued to drop until reaching a stable value (~23 mJm^{-2}), corresponding to the SFE of the alloy, which agrees well with the work on L-PBF-built 316L ASS by Wo et al. [25]. The evolution of $\partial SFP/\partial \varepsilon$ and SFE (calculated) versus temperature curves (Fig. 5a) show that the low temperature significantly reduced the SFE thus accelerated the formation of SFs. The SFE of the 316L ASS decreased almost linearly from 29.2±3.1 mJm^{-2} at 373 K to a very low value of 7.5±1.7 mJm^{-2} at 10 K, with a slope of 0.06 $mJm^{-2}\cdot K^{-1}$. This result agrees well with the SFE-temperature relationship for typical ASSs predicted in Ref. [26]: $SFE^{T} = SFE^{RT} + 0.05(T-293)$, where SFE^{T} and SFE^{RT} are the SFE of the alloy at a designated temperature (*T*) and room temperature, respectively. It is worth noting that the L-PBF 316L ASS showed a higher SFE (23.7±2.2 mJm^{-2} at 293 K) than the annealed 316L ASS, which was only 14.2 mJm^{-2} measured by TEM [27,28], 6.6 mJm^{-2}, and 10 mJm^{-2} by the *ab initio* calculation [29,30]. The increased SFE can be ascribed to two reasons. On one hand, SFE is very sensitive to the variation of chemical composition. The L-PBF can induce the element segregation of Mo and Cr in solidification walls and LAGBs [2,5], which might be reponsible for the increase of SFE. On the other hand, the inhomogeneous distribution of grain size/shape and misorientation gradient produced during L-PBF may also cause the change of SFE. Chen et al. [31] reported the SFE of a high Mn steel increased from 26.0 mJm^{-2} to 34.0 mJm^{-2} as the grain size decreased from ~47 to ~11 μm. According to the thermodynamics simulation [32], the reduced grain size (*d*) can increase the excess of free energy (ΔG_{ex}) required to create SFs: $\Delta G_{ex} = 170.06\exp\left(\frac{-d}{18.55}\right)$. SFE can increase exponentially when *d* decreased to be below 35 μm [33]. The work here demonstrated that SFE of 316L ASS can be tuned by L-PBF via modulating the grain structure and local chemistry. However, further work is needed to establish the relationship between laser processing conditions and SFE.

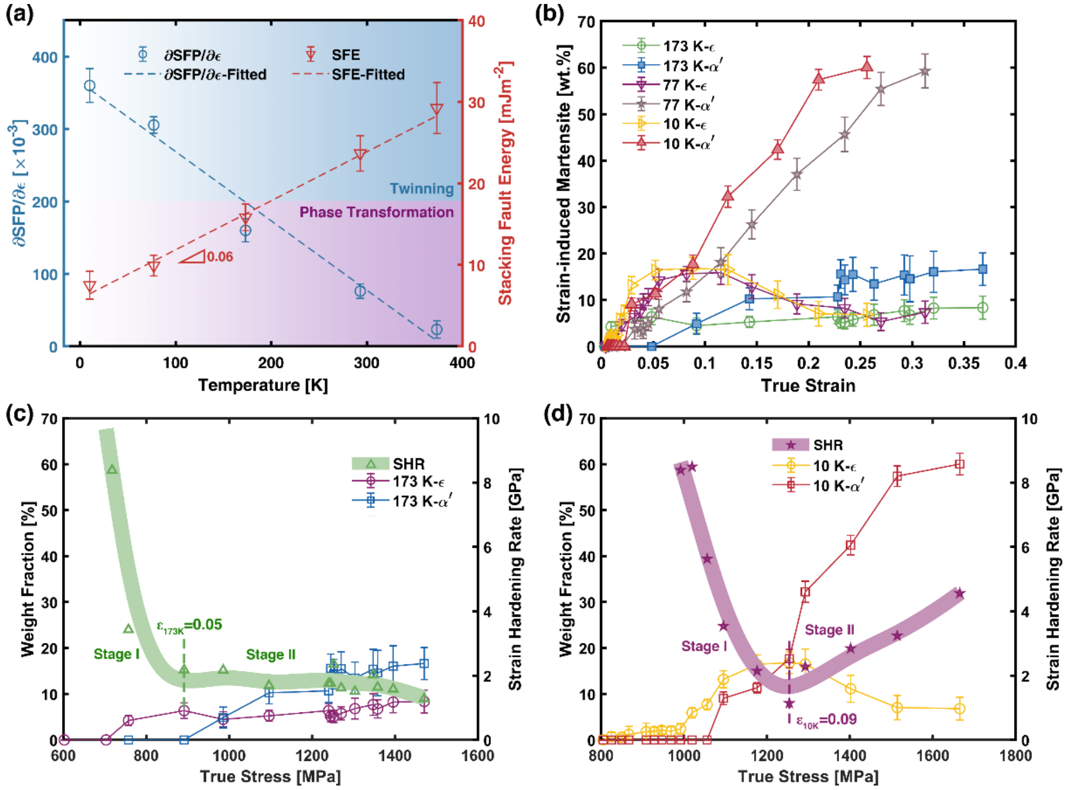

Fig. 5 (a) The temperature dependency of ∂SFP/∂ε and stacking fault energy (SFE) overlapped with SFE-deformation mechanism map; (b) The measured weight fraction of strain-induced ε- and α′-martensite (averaged from tensile and transverse directions) at different deformation temperatures: 173, 77, and 10 K. The strain hardening behaviors and weight fraction of the two martensites (ε and α′) at (c) 173 K and (d) 10 K.

Meanwhile, the measured SFE matches well with the SFE-deformation mechanism map (Fig. 5a). According to the diffraction results (Fig. 3), the strain-induced phase transformation occurred only when temperature decreased to 173 K or lower and SIMT can be significantly promoted by decreasing temperature due to the reduced SFE. The larger dissociation width between partial dislocations provided a higher probability of nucleating martensite. The strain-induced phase transformation occurred only when temperature decreased to be 173 K or lower, as the SFE lowered to 15.8±1.6 mJm^{-2} at 173 K. SIMT was significantly promoted (Fig. 3) as the temperature decreased further.

The weight fraction evolution of the strain-induced ε- and α′-martensite (f_{ε} and $f_{\alpha'}$) at 173, 77 and 10 K were averaged from both loading and transverse directions (Fig. S3 of the Supplementary Materials) and plotted as a function of true strain in Fig. 5b. At the three temperatures, ε-martensite nucleated and grew at very low strain levels (< 0.05), after which f_{ε} maintained at a level of ~15% and decreased slightly at high strains. The formation of α′-martensite started at higher strains (> 0.05). $f_{\alpha'}$ increased almost monotonously with strain at the three temperatures (Fig. 5b), with the rate of increase highest at 10K. $f_{\alpha'}$ of ~60% was achieved at a true strain of ~0.25 at 10 K, which were ~45% at 77 K and ~ 16% at 173 K. The phase weight fraction evolution indicates that two sequences of phase transformation, $\gamma \rightarrow \varepsilon \rightarrow \alpha'$ and $\gamma \rightarrow \alpha'$, were both active during plastic straining. The ε-martensite was first produced and served as an intermediate phase for the following α′-martensite formation. As indicated in Refs. [34,35], the ε/ε interface, including intersection/non-intersection of ε laths, serves as preferable nucleation sites of α′-martensite, which can grow into the interior of the ε-domain and γ matrix at high strain levels, consuming the ε-martensite and triggering the direct transition from γ to α′ [36].

The strengthening behavior of the alloy is closely related with the microstructure and its evolution. The high YS can be originated from its high dislocation density (about 3.6×10^{14} m^{-2}, obtained with modified Williamson-Hall methods [7]), which is close to values reported in L-PBF-built 316L ASS [37]. Conventional 316L ASS showed relatively lower dislocation density of 6.5×10^{13} m^{-2} (after hot forming and solution annealing [17]) and of 2.3×10^{12} m^{-2} (after hot forging and air annealing [18]). Meanwhile, the increase of YS with decreasing temperature can be mainly ascribed to the increase of thermal strengthening effects, which are related to the stress for dislocations to overcome the Peierls stress and pinning effect from solid solute atoms [38].

During plastic deformation, the strengthening effects can be originated from a variety of mechanisms: dislocation multiplication, twinning, and most importantly, SIMT. We plotted the strain hardening rate curves at 173 and 10 K together with martensite weight fraction curves (Fig. 5c and 5d, respectively) to understand effects of SIMT on strain hardening. At 173 K, the rapid drop of SHR in Stage I was relieved slightly before reaching the transition point (true strain of 0.05), during which f_ε reached 6.4±1.7% whereas α′-martensite was about to be produced. During Stage II, both martensites increased slightly (f_ε increased from 6.4±1.7% to 8.3±2.5% and $f_{\alpha'}$ from 0 to 16.6±3.5%, respectively), maintaining the SHR curve at a level of ~ 2 GPa until fracture. At 10 K, a more active phase transformation was observed. During Stage I of SHR curve, both martensites have already formed. f_ε and $f_{\alpha'}$ increased to 16.8±2.4% and 17.7±2.0% at the transition point (true strain of 0.09), respectively. Consequently, the slope of SHR curve at 10 K is less steep than that of 173 K. During Stage II, $f_{\alpha'}$ rapidly increased to 60.0±2.4% while f_ε slightly decreased to 6.8±2.5%, reversing the rapid decreasing curve into a stable increase trend (from 1.1 GPa to 4.5 GPa). This indicates the strong strengthening effects of the α′-martensite. Similar hardening behavior was also observed at 77 K (Fig. S4 of the Supplementary Materials).

The 316L ASS showed excellent strength-ductility combinations at the tested low temperature range. At 373 K, the alloy showed high YS of 562 MPa, UTS of 627 MPa, and large elongation of 55%. At ultralow temperature of 10 K, YS was boosted to 935 MPa and UTS to 1364 MPa while maintaining a large elongation of 34 %. SFE of the L-PBF-built 316L ASS is higher than that of the fully annealed counterparts possibly due to its inhomogeneous distribution of grain size/shape and local composition inhomogeneity. The SFE showed strong temperature dependency, decreasing from 29.2±3.1 mJm^{-2} at 373 K to 7.5±1.7 mJm^{-2} at 10 K, with a slope of 0.06 $mJm^{-2} \cdot K^{-1}$. The decrease of SFE shifted the dominant deformation mechanism from dislocation and twinning (373 and 293 K) to SIMT (173, 77, and 10 K), significantly enhancing the strain hardening effects. The work shows that ASSs fabricated by L-PBF is very promising in achieving desirable strengthening mechanisms and thus premier mechanical performance for cryogenic applications.

Acknowledgements

The authors thank ISIS neutron and muon source (the Rutherford Appleton Laboratory, UK) for providing the beamtime (RB1810732, and RB1920111, and RB2010324) and staff at ENGIN-X beamline for support. BC appreciates the support from the Royal Society International Exchange Grant (IEC\NSFC\191319) and Research Grant (RGS\R2\202122). YW would like to acknowledge the EPSRC (EP/T012250/1) for time.

References

[1] Y. Wang, Y. Zhang, A. Godfrey, J. Kang, Y. Peng, T. Wang, N. Hansen, X. Huang, Cryogenic toughness in a low-cost austenitic steel, Commun. Mater. 2 (2021) 1–10. https://doi.org/10.1038/s43246-021-00149-8.

[2] G.M. Karthik, E.S. Kim, P. Sathiyamoorthi, A. Zargaran, S.G. Jeong, R. Xiong, S.H. Kang, J.W. Cho, H.S. Kim, Delayed deformation-induced martensite transformation and enhanced cryogenic tensile properties in laser additive manufactured 316L austenitic stainless steel, Addit. Manuf. 47 (2021) 102314. https://doi.org/10.1016/j.addma.2021.102314.

[3] D. Herzog, V. Seyda, E. Wycisk, C. Emmelmann, Additive manufacturing of metals, Acta Mater. 117 (2016) 371–392. https://doi.org/10.1016/J.ACTAMAT.2016.07.019.

[4] M.K. Thompson, G. Moroni, T. Vaneker, G. Fadel, R.I. Campbell, I. Gibson, A. Bernard, J. Schulz, P. Graf, B. Ahuja, F. Martina, Design for Additive Manufacturing: Trends, opportunities, considerations, and constraints, CIRP Ann. 65 (2016) 737–760. https://doi.org/10.1016/J.CIRP.2016.05.004.

[5] Y.M. Wang, T. Voisin, J.T. McKeown, J. Ye, N.P. Calta, Z. Li, Z. Zeng, Y. Zhang, W. Chen, T.T. Roehling, R.T. Ott, M.K. Santala, P.J. Depond, M.J. Matthews, A. V. Hamza, T. Zhu, Additively manufactured hierarchical stainless steels with high strength and ductility, Nat. Mater. 17 (2018) 63–70. https://doi.org/10.1038/NMAT5021.

[6] Y. Hong, C. Zhou, Y. Zheng, L. Zhang, J. Zheng, X. Chen, B. An, Formation of strain-induced martensite in selective laser melting austenitic stainless steel, Mater. Sci. Eng. A. 740–741 (2019) 420–426. https://doi.org/10.1016/j.msea.2018.10.121.

[7] L. Tang, L. Wang, M. Wang, H. Liu, S. Kabra, Y. Chiu, B. Cai, Synergistic deformation pathways in a TWIP steel at cryogenic temperatures: In situ neutron diffraction, Acta Mater. 200 (2020) 943–958. https://doi.org/10.1016/j.actamat.2020.09.075.

[8] Y. Wang, B. Liu, K. Yan, M. Wang, S. Kabra, Y.L. Chiu, D. Dye, P.D. Lee, Y. Liu, B. Cai, Probing deformation mechanisms of a FeCoCrNi high-entropy alloy at 293 and 77 K using in situ neutron diffraction, Acta Mater. 154 (2018) 79–89. https://doi.org/10.1016/j.actamat.2018.05.013.

[9] S. Curtze, V.-T.T. Kuokkala, Dependence of tensile deformation behavior of TWIP steels on stacking fault energy, temperature and strain rate, Acta Mater. 58 (2010)

5129–5141. https://doi.org/https://doi.org/10.1016/j.actamat.2010.05.049.

[10] J. Lu, L. Hultman, E. Holmström, K.H. Antonsson, M. Grehk, W. Li, L. Vitos, A. Golpayegani, Stacking fault energies in austenitic stainless steels, Acta Mater. 111 (2016) 39–46. https://doi.org/10.1016/j.actamat.2016.03.042.

[11] S. Huang, H. Huang, W. Li, D. Kim, S. Lu, X. Li, E. Holmström, S.K. Kwon, L. Vitos, Twinning in metastable high-entropy alloys, Nat. Commun. 9 (2018) 2381. https://doi.org/10.1038/s41467-018-04780-x.

[12] M.S. Pham, B. Dovgyy, P.A. Hooper, Twinning induced plasticity in austenitic stainless steel 316L made by additive manufacturing, Mater. Sci. Eng. A. 704 (2017) 102–111. https://doi.org/10.1016/J.MSEA.2017.07.082.

[13] L. Tang, K. Yan, B. Cai, Y. Wang, B. Liu, S. Kabra, M.M. Attallah, Y. Liu, Deformation mechanisms of FeCoCrNiMo0.2 high entropy alloy at 77 and 15 K, Scr. Mater. 178 (2020) 166–170. https://doi.org/10.1016/j.scriptamat.2019.11.026.

[14] B. Cai, B. Liu, S. Kabra, Y. Wang, K. Yan, P.D. Lee, Y. Liu, Deformation mechanisms of Mo alloyed FeCoCrNi high entropy alloy: In situ neutron diffraction, Acta Mater. 127 (2017) 471–480. https://doi.org/10.1016/j.actamat.2017.01.034.

[15] H.M. Rietveld, A profile refinement method for nuclear and magnetic structures, J. Appl. Crystallogr. 2 (1969) 65–71. https://doi.org/10.1107/s0021889869006558.

[16] H.M. Rietveld, Line profiles of neutron powder-diffraction peaks for structure refinement, Acta Crystallogr. 22 (1967) 151–152. https://doi.org/10.1107/s0365110x67000234.

[17] A.A. Coelho, TOPAS and TOPAS-Academic: An optimization program integrating computer algebra and crystallographic objects written in C++: An, J. Appl. Crystallogr. 51 (2018) 210–218. https://doi.org/10.1107/S1600576718000183.

[18] J.K. MACKENZIE, SECOND PAPER ON STATISTICS ASSOCIATED WITH THE RANDOM DISORIENTATION OF CUBES, Biometrika. 45 (1958) 229–240. https://doi.org/10.1093/biomet/45.1-2.229.

[19] H.T. Wang, N.R. Tao, K. Lu, Strengthening an austenitic Fe-Mn steel using nanotwinned austenitic grains, Acta Mater. 60 (2012) 4027–4040. https://doi.org/10.1016/j.actamat.2012.03.035.

[20] M. Naeem, H. He, F. Zhang, H. Huang, S. Harjo, T. Kawasaki, B. Wang, S. Lan, Z. Wu, F. Wang, Y. Wu, Z. Lu, Z. Zhang, C.T. Liu, X.-L. Wang, Cooperative deformation in high-entropy alloys at ultralow temperatures, Sci. Adv. 6 (2020). https://doi.org/10.1126/sciadv.aax4002.

[21] C. Lee, G. Kim, Y. Chou, B.L. Musicó, M.C. Gao, K. An, G. Song, Y.C. Chou, V. Keppens, W. Chen, P.K. Liaw, Temperature dependence of elastic and plastic deformation behavior of a refractory high-entropy alloy, Sci. Adv. 6 (2020) eaaz4748. https://doi.org/10.1126/sciadv.aaz4748.

[22] L. Tang, F.Q. Jiang, J.S. Wróbel, B. Liu, S. Kabra, R.X. Duan, J.H. Luan, Z.B. Jiao, M.M. Attallah, D. Nguyen-Manh, B. Cai, In situ neutron diffraction unravels deformation mechanisms of a strong and ductile FeCrNi medium entropy alloy, J.

Mater. Sci. Technol. 116 (2022) 103–120. https://doi.org/10.1016/j.jmst.2021.10.034.

[23] Z. Wang, A.D. Stoica, D. Ma, A.M. Beese, Diffraction and single-crystal elastic constants of Inconel 625 at room and elevated temperatures determined by neutron diffraction, Mater. Sci. Eng. A. 674 (2016) 406–412. https://doi.org/10.1016/j.msea.2016.08.010.

[24] J.C. Stinville, C. Tromas, P. Villechaise, C. Templier, Anisotropy changes in hardness and indentation modulus induced by plasma nitriding of 316L polycrystalline stainless steel, Scr. Mater. 64 (2011) 37–40. https://doi.org/10.1016/j.scriptamat.2010.08.058.

[25] W. Woo, J.S. Jeong, D.K. Kim, C.M. Lee, S.H. Choi, J.Y. Suh, S.Y. Lee, S. Harjo, T. Kawasaki, Stacking Fault Energy Analyses of Additively Manufactured Stainless Steel 316L and CrCoNi Medium Entropy Alloy Using In Situ Neutron Diffraction, Sci. Rep. 10 (2020) 2–4. https://doi.org/10.1038/s41598-020-58273-3.

[26] A.P. Miodownik, The calculation of stacking fault energies in Fe-Ni-Cr alloys, Calphad. 2 (1978) 207–226. https://doi.org/10.1016/0364-5916(78)90010-X.

[27] S. Lu, Q.M. Hu, B. Johansson, L. Vitos, Stacking fault energies of Mn, Co and Nb alloyed austenitic stainless steels, Acta Mater. 59 (2011) 5728–5734. https://doi.org/10.1016/J.ACTAMAT.2011.05.049.

[28] M. Ojima, Y. Adachi, Y. Tomota, Y. Katada, Y. Kaneko, K. Kuroda, H. Saka, Weak beam TEM study on stacking fault energy of high nitrogen steels, Steel Res. Int. 80 (2009) 477–481. https://doi.org/10.2374/SRI09SP038.

[29] Y. Tian, O.I. Gorbatov, A. Borgenstam, A. V. Ruban, P. Hedström, Deformation Microstructure and Deformation-Induced Martensite in Austenitic Fe-Cr-Ni Alloys Depending on Stacking Fault Energy, Metall. Mater. Trans. A Phys. Metall. Mater. Sci. 48 (2017) 1–7. https://doi.org/10.1007/s11661-016-3839-2.

[30] Z. Dong, W. Li, G. Chai, L. Vitos, Strong temperature – Dependence of Ni -alloying influence on the stacking fault energy in austenitic stainless steel, Scr. Mater. 178 (2020) 438–441. https://doi.org/10.1016/j.scriptamat.2019.12.013.

[31] J. Chen, F.T. Dong, Z.Y. Liu, G.D. Wang, Grain size dependence of twinning behaviors and resultant cryogenic impact toughness in high manganese austenitic steel, J. Mater. Res. Technol. 10 (2021) 175–187. https://doi.org/10.1016/j.jmrt.2020.12.030.

[32] Y.K. Lee, C.S. Choi, Driving force for $\gamma \rightarrow \varepsilon$ martensitic transformation and stacking fault energy of γ in Fe-Mn binary system, Metall. Mater. Trans. A Phys. Metall. Mater. Sci. 31 (2000) 355–360. https://doi.org/10.1007/s11661-000-0271-3.

[33] J.H. Jun, C.S. Choi, Variation of stacking fault energy with austenite grain size and its effect on the MS temperature of $\gamma \rightarrow \varepsilon$ martensitic transformation in Fe-Mn alloy, Mater. Sci. Eng. A. 257 (1998) 353–356. https://doi.org/10.1016/S0921-5093(98)00994-0.

[34] I.R. Souza Filho, A. Dutta, D.R. Almeida Junior, W. Lu, M.J.R. Sandim, D. Ponge,

H.R.Z. Sandim, D. Raabe, The impact of grain-scale strain localization on strain hardening of a high-Mn steel: Real-time tracking of the transition from the γ → ε → α' transformation to twinning, Acta Mater. 197 (2020) 123–136. https://doi.org/10.1016/j.actamat.2020.07.038.

[35] X.S. Yang, S. Sun, H.H. Ruan, S.Q. Shi, T.Y. Zhang, Shear and shuffling accomplishing polymorphic fcc γ → hcp ε → bct α martensitic phase transformation, Acta Mater. 136 (2017) 347–354. https://doi.org/10.1016/j.actamat.2017.07.016.

[36] X.S. Yang, S. Sun, T.Y. Zhang, The mechanism of bcc α′ nucleation in single hcp ε laths in the fcc γ → hcp ε → bcc α′ martensitic phase transformation, Acta Mater. 95 (2015) 264–273. https://doi.org/10.1016/j.actamat.2015.05.034.

[37] K.M. Bertsch, G. Meric de Bellefon, B. Kuehl, D.J. Thoma, Origin of dislocation structures in an additively manufactured austenitic stainless steel 316L, Acta Mater. 199 (2020) 19–33. https://doi.org/10.1016/J.ACTAMAT.2020.07.063.

[38] I.C. Jung, B.C. De Cooman, Temperature dependence of the flow stress of Fe-18Mn-0.6C-xAl twinning-induced plasticity steel, Acta Mater. 61 (2013) 6724–6735. https://doi.org/10.1016/j.actamat.2013.07.042.

List of Tables

Table 1 Parameters used in building 316L ASS with L-PBF

List of Figures

Fig. 1 Initial microstructure of the as-built 316L ASS revealed by EBSD and TEM characterization: (a) inverse pole figure (IPF) map took at the plane perpendicular to the building direction, low angle grain boundaries (LAGBs, 2° < θ < 10°) and high angle grain boundaries (HAGBs, θ > 10°) were shown with white and black lines, respectively; (b) high-resolution kernel average misorientation map showing the orientation gradient, (c) Misorientation distribution of the sample compared with theoretical random misorientation from Ref. [15], and (d) typical bright-field TEM image. BD denotes the building direction.

Fig. 2 Mechanical performance of the 316L ASS at the low temperature range: (a) true stress-strain curves, (b) evolution of mechanical properties with respect to deformation temperature, and (c) strain hardening rate (SHR) plotted with true stress. The SHR

transition points from Stage I to Stage II (ε_{373K}, ε_{293K}, ε_{173K}, ε_{77K}, and $\varepsilon_{10\ K}$) were marked with dashed lines.

Fig. 3 The *in situ* neutron diffraction patterns (loading direction) collected during deforming at different temperatures: (a) 373 K, (b) 293 K, (c) 173 K, (d) 77 K, (e) 10 K, and (f) 10 K, with higher magnification.

Fig. 4 The evolution of (a-e) lattice strain of crystallographic planes {111}, {200}, {220}, {311}, and {222} at the tensile and transverse direction and (f) stacking fault probability evolution during deforming at 373, 293, 173, 77, and 10 K.

Fig. 5 (a) The temperature dependency of $\partial SFP/\partial \varepsilon$ and stacking fault energy (SFE) overlapped with SFE-deformation mechanism map; (b) The measured weight fraction of strain-induced ε- and α′-martensite (averaged from tensile and transverse directions) at different deformation temperatures: 173, 77, and 10 K. The strain hardening behaviors and volume fraction of the two martensites (ε and α′) at (c) 173 K and (d) 10 K.